Topological Thermal Hall Conductance of Even Denominator Fractional States

Arup Kumar Paul[1#], Priya Tiwari[1#], Ron Melcer[2], Vladimir Umansky[1], and Moty Heiblum[1*]

[1] Braun Center for Submicron Research, Department of Condensed Matter Physics, Weizmann Institute of Science, Rehovot, Israel

[2] Qedma Quantum Computing, Tel Aviv, Israel

ABSTRACT

The even denominator fractional quantum Hall (FQH) states ν=5/2 and ν=7/2, have been long predicted to host non-abelian quasiparticles (QPs). The presence of energy-carrying neutral modes cripples customary conductance measurements and thus motivates thermal transport measurements, which already proved to be sensitive to all energy-carrying modes. Each state has a different capacity to carry quanta of heat - as expressed by the so-called: 'central charge' - identifying the state's topological order. While the 'two-terminal' thermal conductance measurements identified the topological orders of abelian and non-abelian QH states, they are prone to partial thermal equilibration among counter-propagating modes. Here, we report a 'four-terminal' thermal Hall conductance measurement, which separately measures the heat carried by the downstream and upstream chiral modes. This measurement is insensitive to thermal equilibration among modes. We verify that the ν=5/2 and ν=7/2 states are non-abelian, supporting a single upstream Majorana mode, thus obeying the Particle-Hole Pfaffian topological order. While current numerical works predict a different central charge, this contribution should motivate further theoretical work.

[#]These authors contributed equally

[*]Corresponding author: moty.heiblum@weizmann.ac.il

The search for quantum states that host non-abelian quasiparticles (QPs), localized or propagating, intensified in the past few years, stemming from their unique characteristics and potential to serve as robust qubits in a noisy environment. Among several proposed implementations, the even-denominator fractional states, the ν=5/2 and ν=7/2, of the Quantum Hall effect (QHE), are the leading candidates [1][12] with numerical calculations predicting an anti-Pfaffian (A-Pf) topological order [3][4]. This order supports a fractional downstream '½ charged mode' and an upstream three Majorana modes (in addition to the downstream integer modes) [2],[7].

In the experimental realm, the ν=5/2 state has been studied extensively. Earlier tunneling measurements pointed at various possible states, such as the A-Pf order [18],[19] or different abelian and non-abelian orders [10][10],[20]. However, more recent heat transport and shot noise measurements pointed to the particle-hole Pfaffian (PH-Pf) order [21-23]. The published works include measurements: (***i***) Two-terminal thermal conductance coefficient k_{2t} of all the edge modes (two integers and the fractions) [19]; (***ii***) Two-terminal thermal conductance coefficient k_{2t} of the isolated fractional mode (charged + Majorana) [22]; (***iii***) Shot noise measurements of the chirality of the isolated fractional mode (charged + Majorana)[23]. The PH-Pf order differs from the A-Pf by supporting a single upstream Majorana mode with *central charge*, c=-1/2 [21][22]. The less explored ν=7/2 state is also expected to be a non-abelian state [16][17]; however, its topological order is still not established.

The 'two-terminal' measurement [24],[25] is based on a known dissipated power in a *small* floating ohmic contact (Source), with its equilibrium temperature related to the *net power* J_{2t} that leaves the contact,

$$J_{2t}=0.5\ k_{2t}\ (T_H^2-T_0^2), \qquad (1)$$

with T_H Source temperature and T_0 Base (Ground) temperature. For a single ballistic chiral abelian mode, the thermal conductance $kT=k_0T=\pi^2k_B^2T/3h$, with T temperature, k_0 *heat quantum*, and k_B and h are Boltzmann and Planck constants, respectively [26],[27]. When the *downstream* edge modes with thermal conductance k_d fully thermally equilibrate with the *upstream* edges modes with thermal conductance k_u, then $k_{2t}=k_d-k_u$. However, when the edge modes do not interact, then $k_{2t}=k_d+k_u$. Consequently, partial thermal equilibration leads to a

value between the two extremes of k_{2t}. For example, in the ν=5/2 state, if a single Majorana mode (carrying heat, $k_0T/2$ [5],[28],[29]) does not thermally equilibrate, the measured thermal conductance would increase by k_0T. Such a lack of equilibration could have led to an apparent PH-Pf order (k_{2t}=2.5k_0 [30]-[36]), while the actual order was A-Pf (k_{2t}=1.5k_0).

To avoid the ambiguity arising from partial equilibration, we employ a configuration that enables the direct determination of the topological thermal Hall conductance, namely, measuring separately the *downstream* and *upstream* heat flows: $J_{down}\sim k_dT$ and $J_{up}\sim k_uT$, with $k_{xy}T=k_dT-k_uT$, thus obtaining the *thermal Hall conductance* (the topological order) [37],[38]. Here, we apply this method to study the two even denominator states, ν=5/2 and ν=7/2.

The devices under test (shown in a false color SEM image in Fig. 1(a)) were fabricated in a 2DEG confined in a GaAs-AlGaAs heterostructure, with short-period superlattice (SPSL) type doping [39],[40]. The 2DEG mobility $\sim 9.1\times10^6 cm^2/V\text{-}S$ and density $2.9\times10^{11}cm^{-2}$, measured at 4.2K in the dark. The QHE response around the two states of interest, measured in a Hall bar, is shown in Fig. 1(b) (see also **Supplementary information (SI-1**)).

The tested devices (Fig. 1(a)) consist of two identical floating ohmic contacts, denoted by L (left) and R (right), each with an area of $\sim 49\mu m^2$. Both contacts are covered with ~25nm thick dielectric HfO_2 followed by a grounded electrode, thus suppressing a possible charging energy [41],[42]. The 2DEG under each floating contact is grooved, thus 'forcing' any incident current to enter the contacts [37],[38]. Contacts L and R are separated by 10μm (or 30μm) of the intermediate 2DEG bulk. A side gate (SG, at the lower part of the bulk), when 'pinched,' guides the edge modes from L to R. When the SG is not biased, the chiral modes flow to the ground. A partial biasing of the SG directs chosen edge modes to the ground. The contacts L & R are also attached to two separate long mesa arms (~120μm long each), with two current sourcing contacts, amplifier contact, and 'cold grounds' (Fig. 1(a)). The amplifier contacts collect the Johnson-Nyquist (J-N) noise to determine the contact's temperature (see **SI-2**) [37].

Each of the floating contacts is heated with a known power supplied by equal and opposite DC currents (+*I* and −*I*) emanating from contacts S1 and S2 (for contact L) or S3 and S4 (for contact R). Each floating contact's potential remains *zero* (eliminating possible emanating shot noise and assuring that the outgoing edge modes carry only the J-N noise), while the

dissipating power is $P_d=I^2R$, with $R=h/\nu e^2$ the quantum Hall resistance. During measurement, the heated floating contact (by DC currents) acts as the *temperature source* (S) (**Fig. SI-2**). The second floating contact is heated by the arrival of the edge modes that leave S, thus acting as a *power meter* (PM). The increased PM temperature is 'translated' to the arrival power from S (**Fig. SI-3**) [37][38]. In the 'downstream configuration,' the floating contact L plays the role of the *Source* while the floating contact R plays the PM role. In the 'upstream configuration,' the functions of L and R are interchanged (**SI-2)**.

We now briefly review the method of obtaining the topological thermal Hall conductance. The arriving downstream heat flow to the PM, J_{down}, and the evacuated heat $J_{out}=J_e+J_\gamma$ (J_e – via edge modes, and J_γ via phonons) leads to net dissipated power in the PM with an equilibrium temperature T_{PM}. The measured T_{PM} is 'converted' to the arriving power, J_{down}, via a separate heating process by a known power (as described above and in **SI-2**). The same procedure is applied when the upstream heat flow, J_{up}, is measured by interchanging the heated and the measuring contacts.

The topological thermal conductance coefficient k_{xy} is found via two measurements, J_{down} and J_{up}, both at the same temperature scale, using,

$$J_{down}-J_{up}=\frac{k_{xy}}{2}\left(T_H^2-T_0^2\right) \ , \qquad (2)$$

where T_H (T_0) is defined above [37]. It is important to stress that thermal equilibration between modes, or lack of it, as well as the contributions of the bulk or due to edge-reconstruction, are eliminated by the subtraction process of J_{down}-J_{up} [37][38]. However, the energy loss of the propagating modes cannot be recovered (moreover, the losses are not necessarily equal in the *down* and *up* directions). Hence, the L-R separation is kept short to minimize heat loss.

We first test the configuration at the well-understood filling ν=2, performing the measurements at the conductance plateau's center (B=6T) on a device with an L-R separation of 10μm. Figure 2(a) shows the measurement configuration with a fully pinched SG gate (V_{SG}=−2V), with two downstream edge modes leaving contact L (Source) and reaching contact R (PM). A less negative gate voltage, V_{SG}=−0.85V (0V), allows only the outer (also the inner) edge modes to reach the ground (Fig. 2(b), see also **SI-3** and **Fig. SI-4b**). Figure 2(c) shows the

dependence of the (calibrated) incoming power J_{down} (to R) as a function of T_L^2-T_0^2 (T_0~11mK), where T_L is the temperature of contact L. The red, blue, and black dots correspond to downstream two modes plus the bulk, one mode plus the bulk, and only the bulk, respectively. With Eq. (1), we find k_d=2.07k_0±0.03k_0 for two propagating edge modes and k_d=1k_0±0.01k_0 for a single edge mode. The heat flow through the bulk and the upstream heat flow are both negligibly small; hence, $k_{xy}(\nu=2)\cong 2k_0$, as expected (Fig. 2(e)).

To verify the impact of bulk conductance on k_{xy}, we tuned the filling away from the center of ν=2 plateau (at 5.6T). Figure 2(d) shows J_{down} versus T_L^2-T_0^2 (T_0~9mK) Here, we find k_d=2.54k_0±0.02k_0 for two edge modes (red circles) and k_d=1.45k_0±0.01k_0 for a single mode (blue circles), both with added contribution of the bulk. The upstream heat flow led to k_u=0.43k_0±0.02k_0 (two modes, green circles) and k_u=0.49k_0±0.01k_0 (one mode, black circles). Consequently, we find k_{xy}=2.11K_0±0.03K_0 and k_{xy}=0.96k_0±0.02k_0 for two and one modes, respectively (Fig. 2(d)). Figure 2(e) summarizes k_{xy} determined at the plateau center (red) and away from it (blue) as a function of downstream edge mode number N (**Fig. SI-4b)**. This 'four terminal' method accurately provides the topological thermal conductance, even in the presence of finite heat flow through the bulk.

Having established the 'four terminal' method's effectiveness, we now focus on the even denominator states. Starting with ν=5/2 and a pinched SG, Fig. 3(a) shows the J_{down} (L to R) versus T_L^2-T_0^2 (T_0~11mK) plots measured at the ν=5/2 plateau's center (B=4.64T). Figure 3(b) shows the J_{up} (R to L) versus T_R^2-T_0^2 with a pinched SG and the bulk conduction with a fully open SG (see also **SI-4**). Figures 3(c-f) present the edge mode configurations between the floating contacts for different SG voltages (**SI-3** and **Fig. SI-4c**).

Table 1 outlines the thermal conductance derived from the plots in Figs. 3(a) & 3(b). Here, the coefficients k_d(N) and k_u(N) represent downstream and upstream thermal conductance for N number of propagating modes (**Fig. SI-4c**). Accordingly, the topological thermal conductance coefficient is $k_{xy}(N)=k_d(N)-k_u(N)$. The bulk contribution k_{bulk}=0.54k_0±0.03k_0 (Fig. 3(b & f)). Finally, we find k_{xy}(3)=2.5k_0±0.07k_0, k_{xy}(2)=1.39k_0±0.05k_0, and k_{xy}(1)=0.29k_0±0.04k_0. The thermal conductance of the isolated inner mode (k_{xy}(1)) is

substantially smaller than its contribution when joined with the integer modes, suggesting an enhanced energy loss of the isolated mode. We will return this issue later.

We repeated the measurements at different locations on the ν=5/2 conductance plateau. The bulk conductance (~G_{bulk}, orange) between the floating contacts is plotted for reference (**Fig. SI-1f**). In Fig. 4(a) we plot $k_d(3)$ (red), $k_u(3)$ (green), and the topological value $k_{xy}(3)$ (blue). We find an average topological thermal conductance across the plateau, $K_{xy}(3)=2.5k_0\pm0.2k_0$. Figure 4(b) presents a comparison between the measured k_{xy} (red) and the expected values (blue) of the PH-Pf order as a function of N.

For the second even-denominator ν=7/2 state we employed a similar device configuration but with an L to R distance of 30μm showing better quality ν=7/2 state (see the comparison in **Fig. SI-1e** and **Fig. SI-1f**). Figure 5(a) shows J_{down} as a function of T_L^2-T_0^2, measured at the center of the plateau (Fig. 1b-inset, B=3.305T). Similar plots of J_{up} and the bulk's contribution are shown in the **SI-4** and **SI 5**. Table 2 summarizes the thermal conductance results for the ν=7/2 state. Here, we find $k_{xy}(4)=3.48k_0\pm0.07k_0$, $k_{xy}(3)=2.40k_0\pm0.05k_0$, $k_{xy}(2)=1K_0\pm0.05K_0$ and $k_{xy}(1)=0.22k_0\pm0.04k_0$. The contribution of the bulk is $k_{bulk}=0.6k_0\pm0.03k_0$, slightly higher than separately measured upstream heat flow, k_u~$0.52K_0\pm0.02K_0$ (used to calculate k_{xy}). The higher k_{bulk} is likely due to a fitting error arising from the relatively noisy data (**SI-5**). Figure 5(b) presents k_{xy} (red) as a function N (**Fig. SI-4d**), with a comparison with the expected values for the PH-Pf order (blue).

In the two studied states, we find a lower thermal conductance than expected of the inner mode(s) when measured after peeling away the integer modes, allegedly contradicting the measured K_{2t} of the most inner mode in the ν=5/2 case [22]. The measurement of k_{2t} relies on the heat that leaves the heated Source contact, while our present measurement of k_d or k_u depends on the heat that reaches the PM, which may suffer from heat loss on its way. We suggest that as we peel off the integer modes by 'opening' the Side Gate (SG), the confining potential gets softer, thus lowering the modes' drift velocity and increasing the inner modes' dwell time – thus possibly increasing its heat loss. This handicap was considered in the design of a relatively short L-to-R separation.

This rather elaborate 'four-terminal' configuration was developed to obtain the *topological order* of fractional states in the Fractional Quantum Hall regime [37],[38]. Moreover, it

overcomes the drawbacks of previously tested 'two-terminal' measurements [24],[25]. It allows employing higher-quality 2DEG (with wider conductance plateaus and lower longitudinal resistance) by eliminating the contribution to heat transfer of the highly intricate doping configuration [21], [37],[39][40]. While the long-standing theoretical predictions of anti-Pfaffian [3]-[5], all our measurements of the ν=5/2 states came up with the Particle-Hole Pfaffian order [21][22],[23]. Finding the same order in the ν=7/2 state may point to more fundamental reasons that prefer the Ph-Pf order for the even denominator states. It will be commendable if new theoretical works address the unavoidable disorder and Landau-level mixing in the GaAs devices [8],[9],[10],[45],[46] . These shortfalls might be overcome in high-quality hBN-encapsulated graphene hosting even denominator states [47].

Acknowledgments

We thank Dima E. Feldman for fruitful discussions. We also thank Sourav Manna and Ankur Das for the valuable discussions and suggestions. M.H. acknowledges the support of the European Research Council under the European Union's Horizon 2020 research and innovation program (grant agreement number 833078).

Author Contribution

A.K.P and P.T designed the experiment, fabricated the devices, performed the measurements, and analyzed the data. R.A.M conceived the experimental setup and guided the initial measurements. M.H supervised the experiment's design, execution, and data analysis. V.U grew the GaAs heterostructures by MBE. All authors contributed to the writing of the manuscript.

Author Statement

The authors declare no competing financial/non-financial interests.

References

[1] Willett, R. et al. Observation of an even-denominator quantum number in the fractional quantum hall effect. Physical review letters 59, 1776 (1987).

[2] Moore, G. & Read, N. Nonabelions in the fractional quantum hall effect. Nuclear Physics B 360, 362–396 (1991).

[3] Morf, R. H. Transition from quantum hall to compressible states in the second Landau level: new light on the ν= 5/2 enigma. Physical review letters 80, 1505 (1998).

[4] Levin, M., Halperin, B. I. & Rosenow, B. Particle-hole symmetry and the pfaffian state. Physical review letters 99, 236806 (2007).

[5] Lee, S.-S., Ryu, S., Nayak, C. & Fisher, M. P. Particle-hole symmetry and the ν= 5 2 quantum hall state. Physical review letters 99, 236807 (2007).

[6] Nayak, C., Simon, S. H., Stern, A., Freedman, M. & Sarma, S. D. Non-abelian anyons and topological quantum computation. Reviews of Modern Physics 80, 1083 (2008).

[7] Stern, A. Non-abelian states of matter. Nature 464, 187–193 (2010).

[8] Storni, M., Morf, R. & Sarma, S. D. Fractional quantum hall state at ν= 5 2 and the moore-read pfaffian. Physical review letters 104, 076803 (2010).

[9] Wójs, A., T˝oke, C. & Jain, J. K. Landau-level mixing and the emergence of pfaffian excitations for the 5/2 fractional quantum hall effect. Physical review letters 105, 096802 (2010).

[10] Zucker, P. & Feldman, D. Stabilization of the particle-hole Pfaffian order by landau-level mixing and impurities that break particle-hole symmetry. Physical Review Letters 117, 096802 (2016).

[11] Rezayi, E. H. Landau level mixing and the ground state of the ν= 5/2 quantum hall effect. Physical Review Letters 119, 026801 (2017).

[12] Antoniˇ c, L., Vuˇciˇceviˇ c, J. & Milovanoviˇ c, M. Paired states at 5/2: Particle-hole pfaffian and particle-hole symmetry breaking. Physical Review B 98, 115107 (2018).

[13] Pan, W. et al. Strongly anisotropic electronic transport at landau level filling factor ν= 9/2 and ν= 5/2 under a tilted magnetic field. Physical Review Letters 83, 820 (1999).

[14] Willett, R. L., Pfeiffer, L. N. & West, K. Measurement of filling factor 5/2 quasiparticle interference with observation of charge e/4 and e/2 period oscillations. Proceedings of the National Academy of Sciences 106, 8853–8858 (2009).

[15] Liu, Y. et al. Evolution of the 7/2 fractional quantum hall state in two-subband systems. Physical review letters 107, 266802 (2011).

[16] Feldman, D. E. & Halperin, B. I. Fractional charge and fractional statistics in the quantum hall effects. Reports on Progress in Physics 84, 076501 (2021).

[17] Willett, R. et al. Interference measurements of non-abelian e/4 & abelian e/2 quasiparticle braiding. Physical Review X 13, 011028 (2023).

[18] Radu, I. P. et al. Quasi-particle properties from tunneling in the ν= 5/2 fractional quantum hall state. Science 320, 899–902 (2008).

[19] Lin, X., Dillard, C., Kastner, M., Pfeiffer, L. & West, K. Measurements of quasiparticle tunneling in the υ= 5 2 fractional quantum hall state. Physical Review B 85, 165321 (2012).

[20] Baer, S. et al. Experimental probe of topological orders and edge excitations in the second Landau level. Physical Review B 90, 075403 (2014).

[21] Banerjee, M. et al. Observation of half-integer thermal hall conductance. Nature 559, 205–210 (2018).

[22] Dutta, B., Umansky, V., Banerjee, M. & Heiblum, M. Isolated ballistic non-abelian interface channel. Science 377, 1198–1201 (2022).

[23] Dutta, B. et al. Distinguishing between non-abelian topological orders in a quantum hall system. Science 375, 193–197 (2022).

[24]Jezouin, S. et al. Quantum limit of heat flow across a single electronic channel. Science 342, 601–604 (2013).

[25]Srivastav, S. K. et al. Universal quantized thermal conductance in graphene. Science Advances 5, eaaw5798 (2019).

[26]Kane, C. & Fisher, M. P. Quantized thermal transport in the fractional quantum hall effect. Physical Review B 55, 15832 (1997).

[27]Cappelli, A., Huerta, M. & Zemba, G. R. Thermal transport in chiral conformal theories and hierarchical quantum hall states. Nuclear Physics B 636, 568–582 (2002).

[28]Nomura, K., Ryu, S., Furusaki, A. & Nagaosa, N. Cross-correlated responses of topological superconductors and superfluids. Physical review letters 108, 026802 (2012).

[29]Sumiyoshi, H. & Fujimoto, S. Quantum thermal hall effect in a time-reversal-symmetry-broken topological superconductor in two dimensions: approach from bulk calculations. Journal of the Physical Society of Japan 82, 023602 (2013).

[30]Read, N. & Green, D. Paired states of fermions in two dimensions with breaking of parity and time-reversal symmetries and the fractional quantum hall effect. Physical Review B 61, 10267 (2000).

[31]Simon, S. H., Ippoliti, M., Zaletel, M. P. & Rezayi, E. H. Energetics of pfaffian–anti-pfaffian domains. Physical Review B 101, 041302 (2020).

[32]Simon, S. H. Interpretation of thermal conductance of the ν= 5/2 edge. Physical Review B 97, 121406 (2018).

[33]Feldman, D. Comment on âinterpretation of thermal conductance of the ν= 5/2 edgeâ. Physical Review B 98, 167401 (2018).

[34]Simon, S. H. & Rosenow, B. Partial equilibration of the anti-pfaffian edge due to Majorana disorder. Physical Review Letters 124, 126801 (2020).

[35] Hein, M. & Spånslätt, C. Thermal conductance and noise of Majorana modes along interfaced ν= 5 2 fractional quantum hall states. Physical Review B 107, 245301 (2023).

[36] Manna, Sourav, et al. "Full Classification of Transport on an Equilibrated 5/2 Edge." arXiv preprint arXiv:2212.05732 (2022).

[37] Melcer, R. A., Konyzheva, S., Heiblum, M. & Umansky, V. Direct determination of the topological thermal conductance via local power measurement. Nature Physics 19, 327–332 (2023).

[38] Melcer, R. A. et al. Heat conductance of the quantum hall bulk. arXiv preprint arXiv:2306.14977 (2023).

[39] Umansky, V. et al. Mbe growth of ultra-low disorder 2deg with mobility exceeding 35× 106 cm2/v s. Journal of Crystal Growth 311, 1658–1661 (2009).

[40] Umansky, V. Y. & Heiblum, M. Mbe growth of high-mobility 2deg. In Molecular Beam Epitaxy: From research to mass production, 121–137 (Elsevier Science, 2013).

[41] Slobodeniuk, A. O., Levkivskyi, I. P. & Sukhorukov, E. V. Equilibration of quantum hall edge states by an ohmic contact. Physical Review B 88, 165307 (2013).

[42] Sivre, E. et al. Heat coulomb blockade of one ballistic channel. Nature Physics 14, 145–148 (2018).

[43] Venkatachalam, V., Yacoby, A., Pfeiffer, L. & West, K. Local charge of the ν= 5/2 fractional quantum hall state. Nature 469, 185–188 (2011).

[44] Bid, A. et al. Observation of neutral modes in the fractional quantum hall regime. Nature 466, 585–590 (2010).

[45] Das, S., Das, S. & Mandal, S. S. Anomalous reentrant 5/2 quantum hall phase at moderate landau-level-mixing strength. Physical Review Letters 131, 056202 (2023).

[46] Herviou, L. & Mila, F. Possible restoration of particle-hole symmetry in the 5/2-quantized Hall state at small magnetic field. Physical Review B 107, 115137 (2023).

[47]Huang, K. et al. Valley isospin controlled fractional quantum hall states in bilayer graphene. Physical Review X 12, 031019 (2022).

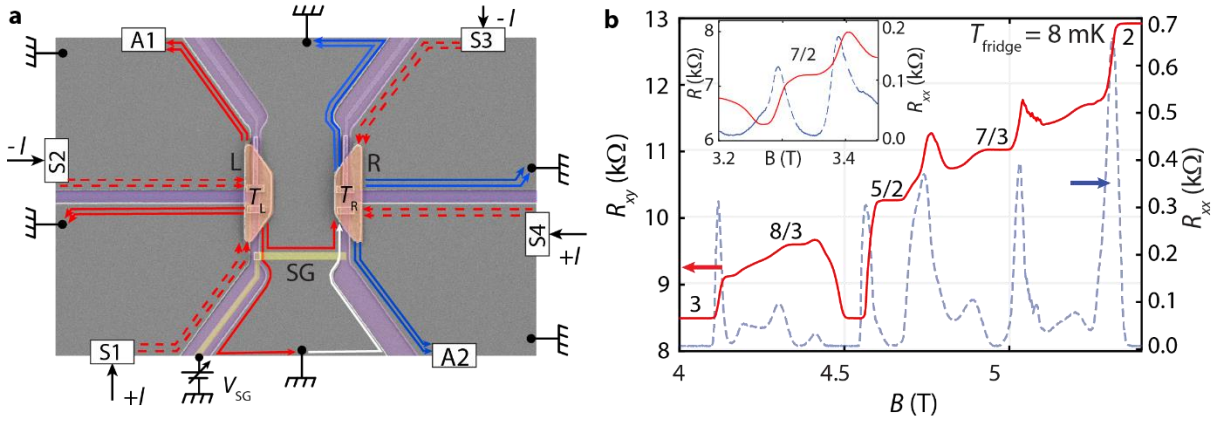

Figure 1: The device and the quantum Hall response. (a) An SEM image of the device showing the floating contacts (orange), **L** (temperature T_L), and R (temperature T_R), the continuous side gate, **SG** (yellow, charged by V_{SG}), and the mesa arms (grey), defined by etching grooves in the GaAs (purple). The arrowed lines represent the QH edge modes. Red arrowed dashed lines show current-carrying edge modes (injected from **S1** and **S2** or **S3** and **S4**) that heat the floating contacts. Solid red and blue lines represent the outgoing edge modes from contacts **L** and **R**. **A1** and **A2** amplifiers' contacts. **(b)** R_{xy} (red) and R_{xx} (dashed blue) are plotted as a function of the magnetic field B (fridge temperature, T_{fridge}=8mK). Plateaus and minima of ν=7/3, 5/2, and 8/3 are distinct. The inset shows R_{xy} (red) and R_{xx} (dashed blue) vs. B around the ν=7/2 plateau.

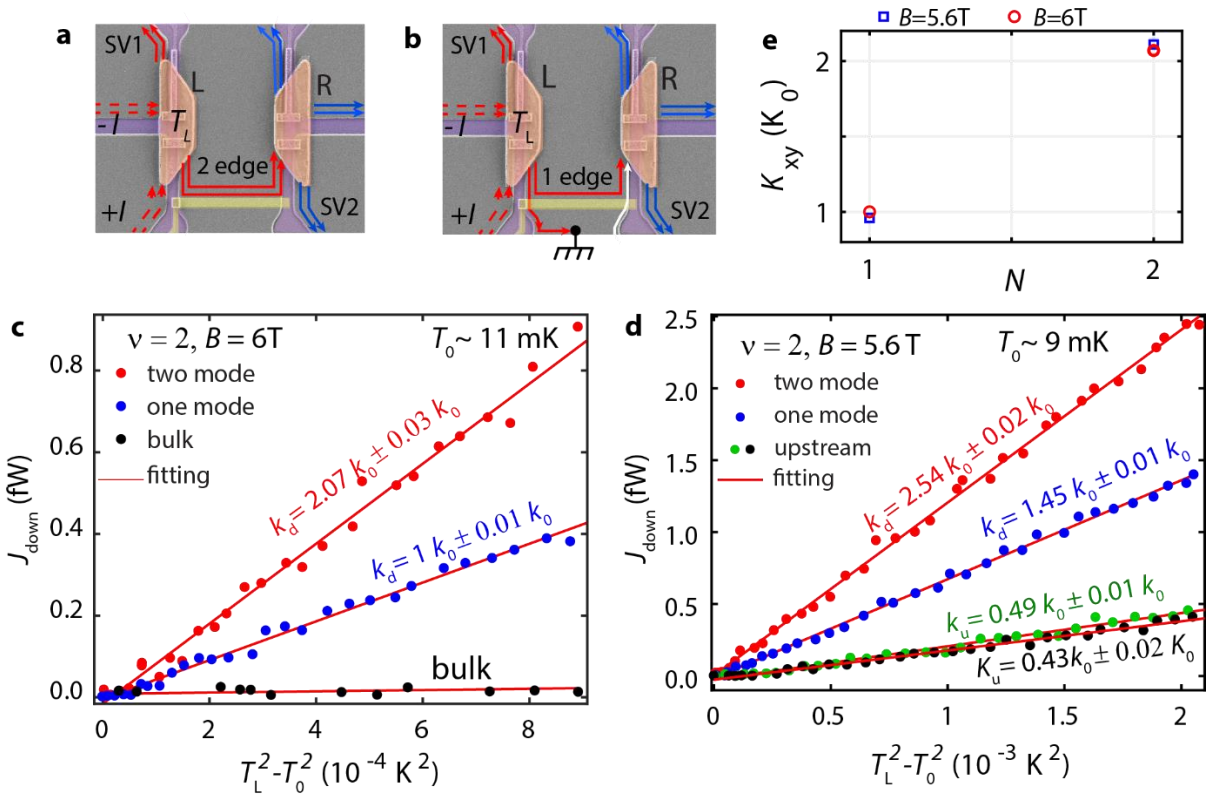

Figure 2: Thermal conductance of ν=2: For downstream heat flow, contact **L** acts as the Source, and contact **R** acts as the PM. Currents ***+I*** and ***–I*** heat contact **L**. The temperature of the two floating contacts is determined by measuring the spectral density of the Johnson-Nyquist noise, denoted by **SV1** and **SV2**. **(a)** Configuration for downstream heat flow measurement with two edge modes (solid red lines) carry heat from **L** to **R** (V_{SG}=−2V). **(b)** Configuration for the inner edge mode reaching contact **R**, while the outer edge mode is diverted to Ground (V_{SG}=−0.85V). **(c)** Downstream heat flow J_{down} arrives at contact **R** and heats the contact. The J_{down} is plotted as a function of T_L^2-T_0^2 (T_0~11mK, electron temperature). The red, blue, and black colors correspond to heat conduction by two modes, one mode and only the bulk, respectively. Solid red lines are the linear fit to the data. **(d)** J_{down} vs. T_L^2-T_0^2 response away from the plateau's center (at B=5.6T). Red and blue colors correspond to downstream heat flow by two and one edge modes, respectively. The green and black colors represent upstream heat flow for the same two configurations. Here, finite upstream heat flow is via the bulk. **(e)** k_{xy} as function number of edge mode (N) determined from k_d and k_u values at 6T (red circles) and 5.6T (blue square). For clarity, we have removed

the error bars. k_{xy} has the same values in both cases, effectively eliminating the bulk heat conduction.

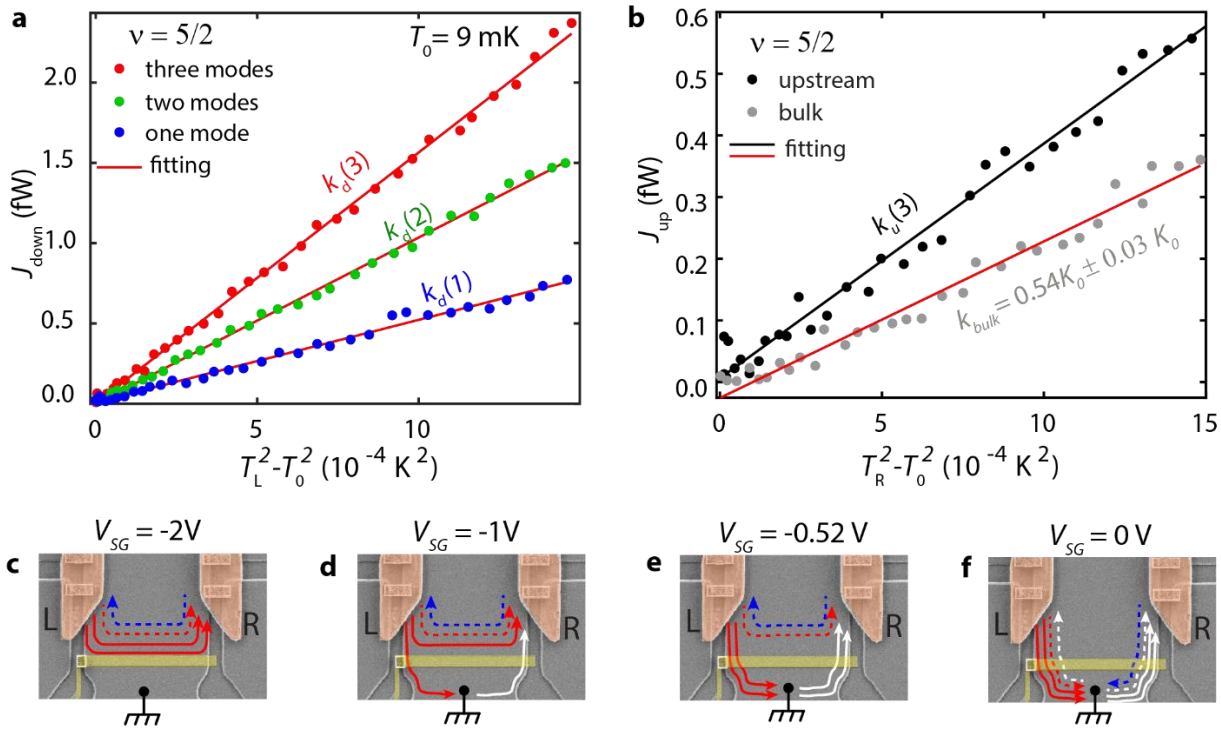

Figure 3: Thermal conductance of ν =5/2. (a) Downstream power flow J_{down} leaves the heated contact L and reaches contact **R** plotted vs. T_L^2-T_0^2 (T_0=9mK, electron temperature). The red, green, and blue data points are for all edge modes, two outer and the innermost fractional mode, respectively. The downstream heat conductance k_d(N=3,2,1) is determined from the linear fittings shown by the solid lines and are given in Table 1. **(b)** Upstream heat flow J_{up} are measured by changing the roles of **L** and **R** with all modes participating, and plotted as a function of T_R^2-T_0^2 (in black), while the bulk itself is in grey. Error bars show a statistical error. **(c)-(f)** Different configurations of edge modes propagation between **L** & **R**: **(c)** Fully pinched **SG** (V_{SG}=-2V), **(d)** and **(e)** Partially pinched **SG** with one (V_{SG}=-1V) and two (V_{SG}=-0.52V) edge modes diverted to ground. **(f)** Fully open **SG** (V_{SG} =0V). The arrows indicate edge modes: solid red for downstream integer modes, dashed red for downstream fractional mode, and blue dashed arrow for upstream modes. White arrows show edge modes emanating from the ground.

ν	N	k_d(N)	k_u(N)	k_{xy}(N)	k_{bulk}
5/2	all modes, N=3	$k_d(3) = 3.30\ k_0 \pm 0.05\ k_0$	$\sim 0.8\ k_0 \pm 0.02\ k_0$	$k_{xy}(3) = 2.5\ k_0 \pm 0.07\ k_0$	$\sim 0.54\ k_0 \pm 0.03\ k_0$
	inner modes, N=2	$k_d(2) = 2.19\ k_0 \pm 0.03\ k_0$		$k_{xy}(2) = 1.39\ k_0 \pm 0.05\ k_0$	
	innermost fractional mode, N=1	$k_d(1) = 1.09\ k_0 \pm 0.02\ k_0$		$k_{xy}(1) = 0.29\ k_0 \pm 0.04\ k_0$	

Table 1: Downstream and upstream thermal conductance k_d(N) and k_u(N) and topological thermal Hall conductance k_{xy}(N) as a function of the number of downstream charged edge modes (N) between the floating contacts L and R. k_{bulk} is the bulk thermal conductance.

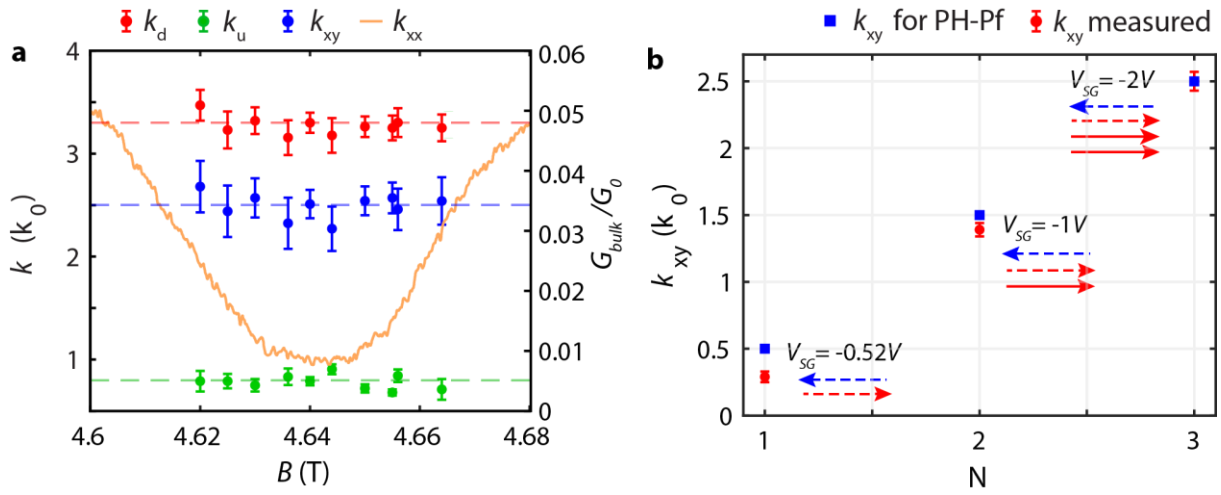

Figure 4: Summary of data of ν=5/2. (a) Bulk conductance between L and R G_{bulk} (orange) in units of G_0, k_{xy} (blue), k_d (red), and k_u (green) - as function magnetic field (B) around the minima of G_{bulk}. **(b)** k_{xy} as a function of the number of edge modes (N) propagating downstream between L and R. The blue squares are the expected values of K_{xy} of the PH-Pf order. The arrows show the edge structures of the PH-Pf order at different V_{SG}. Solid and Dashed red arrows represent downstream integer and ½ fractional mode, respectively. Blue dashed arrows show upstream Majorana mode. The error bars in the figures correspond to statistical error. Note the more significant deviation at N=1.

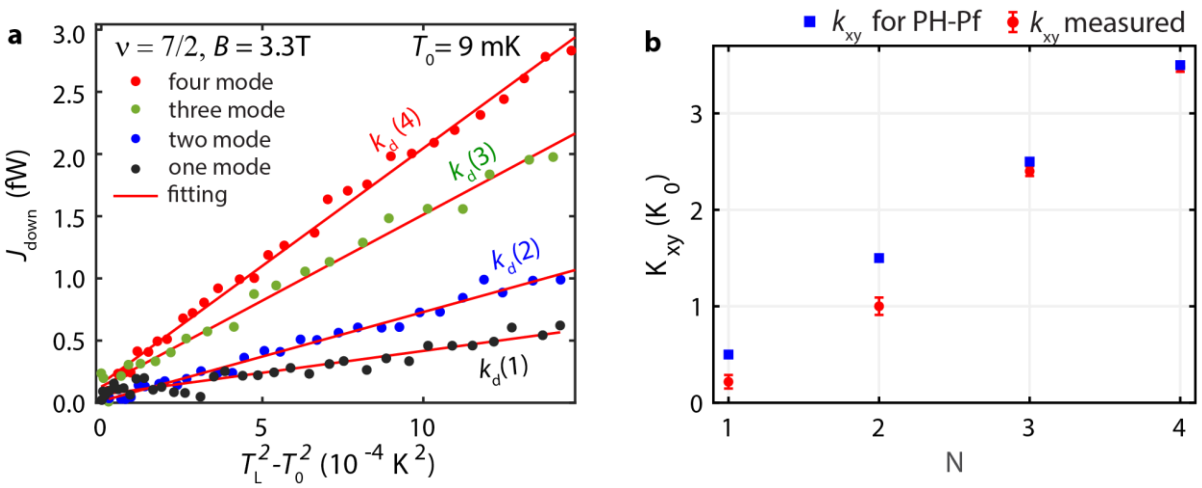

Figure 5: Thermal conductance of ν=7/2. (a) J_{down} vs. T_L^2-T_0^2 plots at the center of ν=7/2 plateau at 3.3T (T_0=9mK, electron temperature). The red, green, blue, and black data points correspond to all edge modes: inner three, inner two, and innermost fractional mode. The corresponding downstream heat conductance k_d(N=1,2,3) are shown in Table 2. **(b)** k_{xy} (red error bars) as a function of the number of downstream edge modes (N) propagating from L to R at ν=7/2. The blue squares are the expected values of k_{xy} of the PH-Pf order. The error bars in the figures correspond to statistical error. Note the more significant deviations for N=1,2.

ν	N	k_d (N)	k_u (N)	k_{xy}(N)	k_{bulk}
7/2	all modes, N=4	$k_d(4) = 4\ k_0 \pm 0.05\ k_0$	~ 0.52 $k_0 \pm 0.02\ k_0$	$K_{xy}(4) = 3.48\ k_0 \pm 0.07\ k_0$	~ 0.6 $k_0 \pm 0.04\ k_0$
	inner modes, N=3	$k_d(3) = 2.92\ k_0 \pm 0.07\ k_0$		$K_{xy}(3) = 2.40\ k_0 \pm 0.05\ k_0$	
	inner two modes, N=2	$k_d(2) = 1.51\ k_0 \pm 0.03\ k_0$		$K_{xy}(2) = 1\ k_0 \pm 0.05\ k_0$	
	innermost fractional mode, N=1	$k_d(1) = 0.74\ k_0 \pm 0.04\ k_0$		$K_{xy}(1) = 0.22\ k_0 \pm 0.04\ k_0$	

Table 2: For ν=7/2, downstream and upstream thermal conductance k_d(N) and k_u(N) and topological thermal Hall conductance k_{xy}(N) as a function of number downstream charged edge modes (N). k_{bulk} stands for bulk's thermal conductance.

Supplementary Information

Topological Thermal Hall Conductance of Even Denominator Fractional States

Arup Kumar Paul[1#], Priya Tiwari[1#], Ron Melcer[2], Vladimir Umansky[1], and Moty Heiblum[1*]

[1] Braun Center for Submicron Research, Department of Condensed Matter Physics, Weizmann Institute of Science, Rehovot, Israel

[2] Qedma Quantum Computing, Tel Aviv, Israel

SI-1: Quantum Hall response of the thermal conductance devices

Figure SI-1a shows R_{xy} (in red) and R_{xx} (in blue) as function of magnetic field B around the ν=7/2 plateau from the Hall bar sample. In contrast to the Hall bar, the thermal conductance device's geometry doesn't permit direct measurement of longitudinal resistance (R_{xx}) [1,2]. Instead, we rely on bulk leakage current (ΔI) between floating contacts (L and R) to identify the minima of bulk conductance G_{bulk} (equivalent to minima of R_{xx}). Figure SI-1b illustrates the low-frequency (~17Hz) setup to measure G_{bulk} between the floating contacts. An ac current (I_{ac}) is injected from source contact S1 and in absence of any bulk leakage it is carried to the floating contact L by the edge modes denoted with red dashed arrows. Here, the current splits between the outgoing edge modes (colored orange). In each arm the outgoing current (I_{out}) is determined by the voltage drop (V_m) on a separate ohmic contact connecting the outgoing edge modes to the ground, like the probe V1 in the top-left arm. V_m given by,

$$V_m = I_{out} R_H \qquad \text{(SI-1)}$$

where R_H is the quantum Hall resistance. We find $I_{out} \sim \frac{I_{ac}}{3}$ for all the arms at the QH plateau centers, even for the ν=7/2 and ν=5/2 states, with finite bulk conductance. The equal splitting of current indicates significantly small or absent bulk conductance at the plateau centers. Also, equal current-splitting results in a voltage drop at the floating contact L, given by,

# These authors contributed equally

*Corresponding author: moty.heiblum@weizmann.ac.il

$$V_L \sim \frac{I_{ac}}{3} R_H \qquad \text{(SI-2)}$$

Similarly, in the presence of bulk leakage, any small current ΔI reaching the other floating contact R induces a voltage drop at R,

$$V_R \sim \frac{\Delta I}{3} R_H. \qquad \text{(SI-3)}$$

This drop is measured by the voltage probe V2 (at the bottom-right mesa arm). The magnitude of ΔI depends on the difference, V_L-V_R and bulk resistance (R_{bulk}), between the floating contacts, hence,

$$V_L\text{-}V_R \sim \Delta I\, R_{bulk}\ . \qquad \text{(SI-4)}$$

Using **Eqs. SI-1** to **SI-3** we get,

$$R_{bulk} = (R_H/3)(V_L\text{-}V_R)/V_R \sim (R_H/3)(V_L/V_R) \sim$$

$$\sim \left(\frac{R_H{}^2}{9}\right)\left(\frac{I_{ac}}{V_R}\right), \qquad \text{(SI-5)}$$

Here we have ignored the second term on the right-hand side since the measured V_L is two orders larger than V_R. Finally, **Eqs. SI-5** leads to,

$$G_{bulk} = \frac{1}{R_{bulk}} = \frac{9}{R_H{}^2}\left(\frac{V_R}{I_{ac}}\right). \qquad \text{(SI-6)}$$

The Figs SI-1c, SI-1d, and SI-1e display the measured G_{bulk} (in blue) as a function of the magnetic field (B) for filling factors ν=2, ν=5/2, and ν=7/2, respectively in the device with 10μm L-R separation. Additionally, two-terminal Hall resistance (R_{2t}) traces (in red to black) measured at different voltage probes or current injection contacts in the sample are also shown. R_{2t} is determined by measuring the voltage drop at the contacts while injecting a known current. For the integer ν=2 state, G_{bulk} remains zero throughout the plateau (Fig. SI-1c). In the ν=5/2 state, R_{2t} traces exhibit clear plateaus for different contacts (Fig. SI-1d). The G_{bulk} reaches a minimum of ~0.01G_0, near the plateau's center at B=4.64T, while increasing rapidly away from the center of the plateau. The ν=7/2 state, however, is not well developed, as seen in the R_{2t} and G_{bulk} responses in Fig. SI-1e. The Figure SI-1d shows the ν=7/2 state's

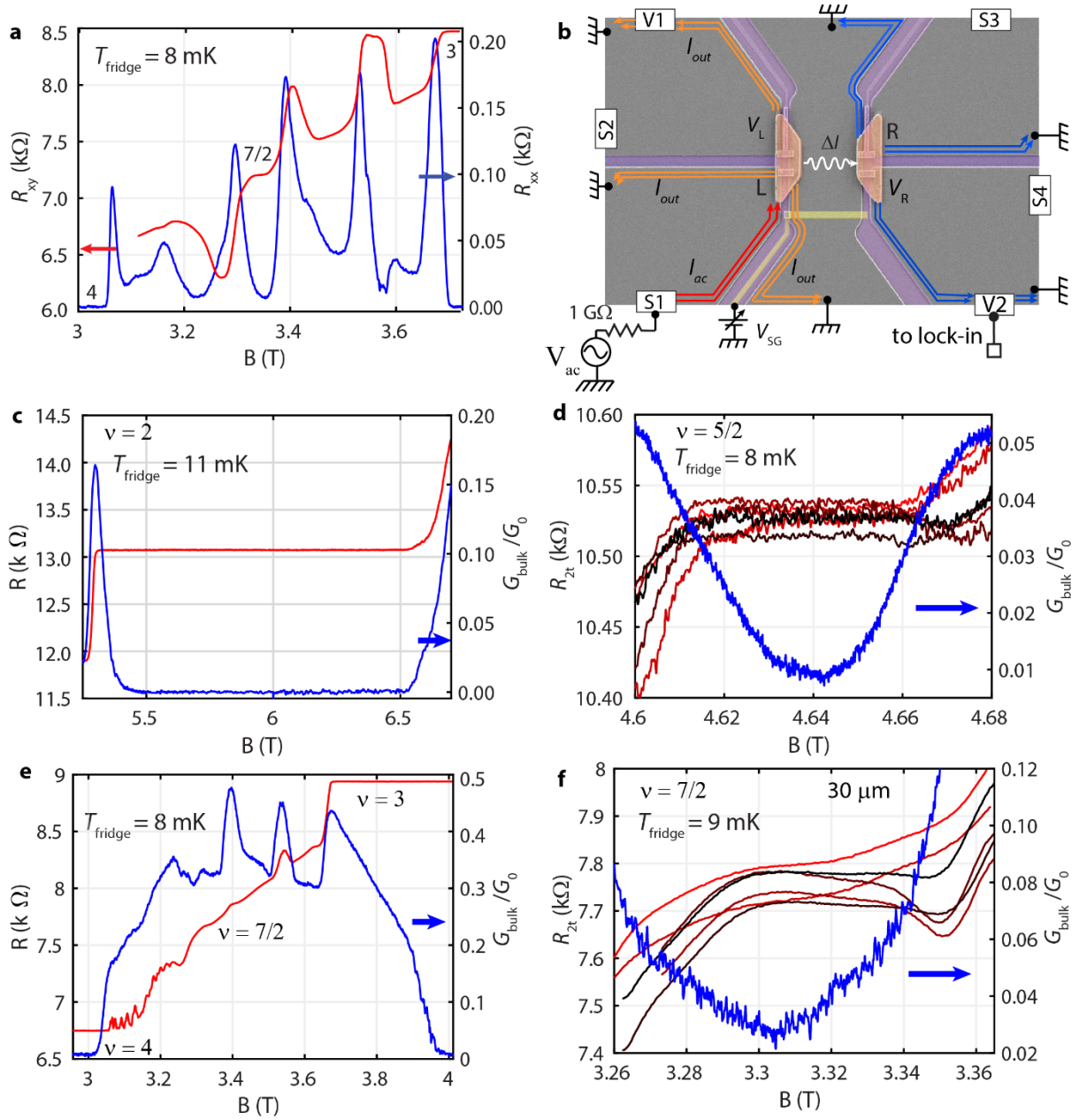

Figure SI-1: Quantum Hall responses - (a) Quantum Hall response around the ν=7/2 state in the Hall bar device. **(b)** Measurement configuration for determining bulk conductance G_{bulk} between the floating contacts. The gate SG is fully open, diverting all edge modes from contact L to ground. **(c)-(e)** Two-terminal quantum Hall resistance R_{2t} and G_{bulk} as functions of the applied field B at ν=2, ν=5/2, and ν=7/2 in the device with a 10μm separation between the floating contacts. R_{2t} traces measured from different contacts are shown by the colors red to black. The measured G_{bulk} is depicted in blue. **(f)** R_{2t} and G_{bulk} vs. B responses around the ν=7/2 state in the device with a 30μm separation between the floating contacts.

response in the device with 30μm separation between the floating contacts. In this device, the ν=7/2 state is well developed with R_{2t} plateaus visible in different contacts. Here, G_{bulk} shows a clear minimum of ~0.03G_0 at 3.305 T, prompting us to check the thermal conductance of ν=7/2 state in this device.

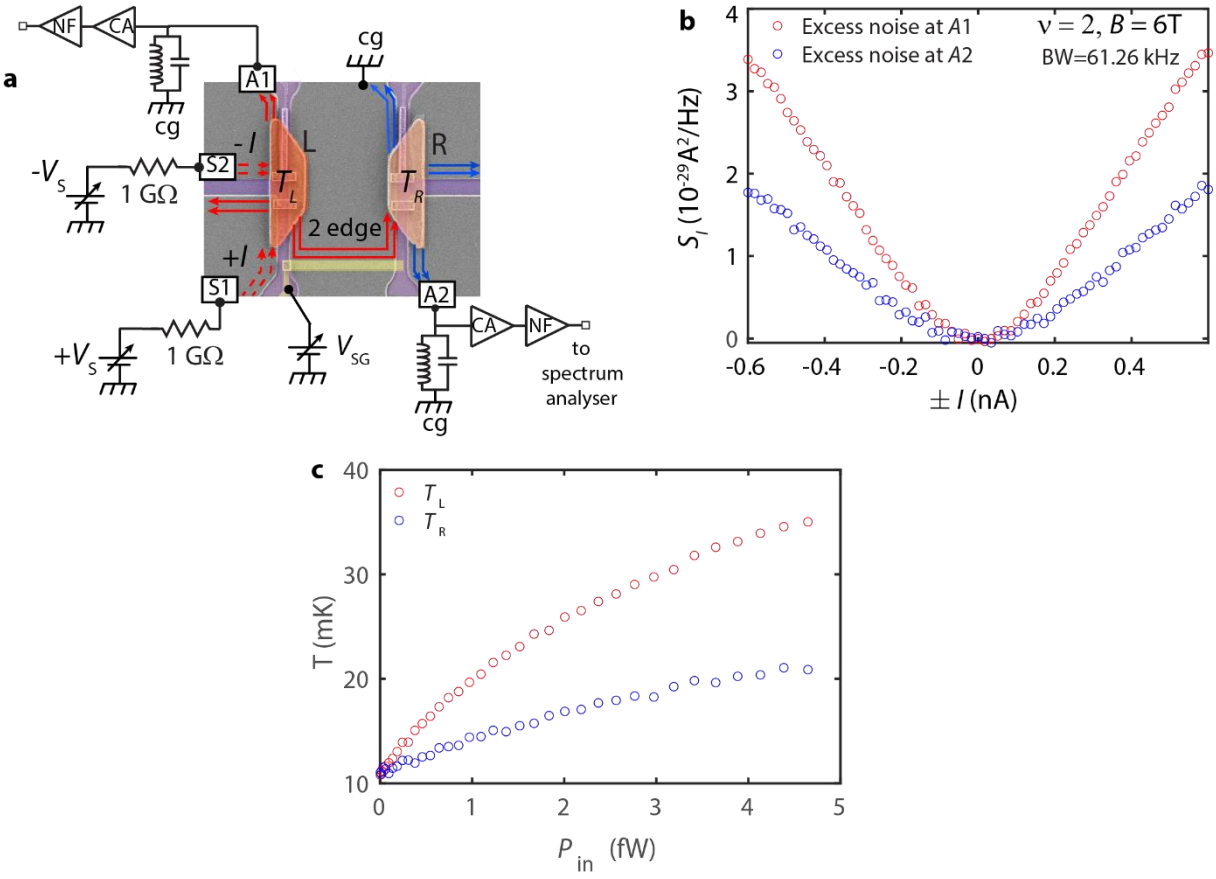

Figure SI-2: Excess thermal noise measurement - (a) Setup to measure excess thermal noise from the floating contacts: the contact L (dark red) heated with known electrical power acts as temperature source, while the contact R (light red) heats up from arriving power from the source, thus acts as power meter (PM). **(b)** Measured excess noise (S_I) from the floating contacts plotted against injected current (I) to the source. The colors red and blue are for the source (contact L) and power meter (contact R) noises, respectively. **(c)** Temperatures T_L (red) and T_R (blue) of the floating contacts determined from S_I using **Eqs. SI-7**, as function of applied power P_{in} to the source.

SI-2. Thermal conductance measurement

There are two steps in the thermal conductance measurement [1,2]: 1) J-N thermal noise measurement and 2) Power-Meter (PM) calibration. The following sections describe the two steps using the downstream thermal conductance measurement at ν=2 as an example. Note for the upstream case, the roles of the floating contacts are reversed.

Thermal noise measurement: In this step, one of the floating contacts is directly heated with a known electrical power, functioning as a *temperature source*. The other floating contact heats up due to incoming power carried by the arriving edge modes from the temperature source or the bulk. The latter contact is labeled as the *power meter* (PM). The heating of both contacts results in outgoing edge modes carrying excess J-N noise, subsequently converted to the temperature of the floating contacts.

Figure SI-2a shows the setup where the floating contacts L and R act as the *source* and PM, respectively. Contact L is heated with the equal and opposite currents (dc) *+I* and *-I* injected from contacts S1 and S2 and are carried by the edge modes denoted as red dashed arrows. The dc currents are injected using the 1GΩ resistances in series with the sample and the dc voltage source V_s. The injected currents cause net power dissipation I^2R_H at the floating contact L. At a steady state, the dissipated power equals the net outgoing power carried by the outgoing edge modes (red solid lines). By applying a suitable gate voltage V_{SG}, the edge modes in the middle arm are directed to contact R, increasing its temperature. The resulting excess J-N thermal noise (S_I) is measured by amplifiers connected to the contacts A1 and A2 for L and R, respectively. The amplifier lines play as an LC tank circuit, followed by a cold amplifier (CA) at a temperature 4K followed by a room temperature (NF) amplifier. Noise is measured at the LC resonance frequencies (~632 kHz and ~717 kHz for L and R, respectively), with a bandwidth (BW) of ~61.3kHz. Figure SI-2b presents the measured excess J-N noise S_I from the two floating contacts as a function of the injected current *I* when contact L is heated. Figure SI-2c presents the excess noise being converted to the temperature of the floating

contacts (T_L and T_R) as a function of dissipated power ($P_{in}=I^2R_H$). We use the following expression for the conversion [1,2] ,

$$S_I=2k_B\Delta T\, G^* \qquad \text{(SI-7)}$$

where k_B is the Boltzmann constant, ΔT (T_L-T_0 or T_R-T_0) is the excess temperature of the floating contacts and G^* is given by:

$$G^* = \frac{G_{S\to A}G_{S\to G}}{G_{S\to A}+G_{S\to G}}, \qquad \text{(SI-8)}$$

with $G_{S\to A}$ is conductance between source and amplifier contact, and $G_{S\to G}$ is the conductance between the source and cold grounds.

Power-meter calibration: In this step, the PM is heated with known electrical power to establish its temperature vs. input power response, labeled as the calibration curve. Leveraging this curve, the PM temperature (T_R) from the preceding step is translated to arriving power. With the exception of heating the PM instead of the source, the rest of the calibration step is identical to the noise measurement step.

Figure SI-3a, illustrates the setup for generating the calibration curve for contact R. In this configuration, the contact R (rather than L) is heated with the equal and opposite dc currents *+I* and *-I*, injected via the source contacts S3 and S4, respectively. The excess noise (S_I) for both floating contacts, resulting from heating of contact R are presented in Figure SI-3b. Similar to the previous step, the excess noise responses are converted to temperatures of the floating contacts using **Eqs. SI-7**. Figure SI-3c shows the resultant temperatures T_R and T_L as function of the input power P_{in} to contact R. Here, the T_R vs. P_{in} response represents the calibration curve. We use this calibration curve to determine the input power to PM corresponding to the measured PM temperatures from the previous step. In Figure SI-3d, the calibration curve is depicted in red, with green squares representing the measured PM (contact R) temperatures when the source (contact L) is heated. The power arriving to the PM ($P_{S\text{-}PM}$, from source) corresponding to the green squares is plotted against input power P_{in}^{S} to the source L in Figure SI-3e. Finally, Figure SI-3f shows $P_{S\text{-}PM}$ vs. $T_L^2 - T_0^2$ plot for the determination of thermal

conductance. In this plot T_L corresponds to the source temperature when it is heated with known power.

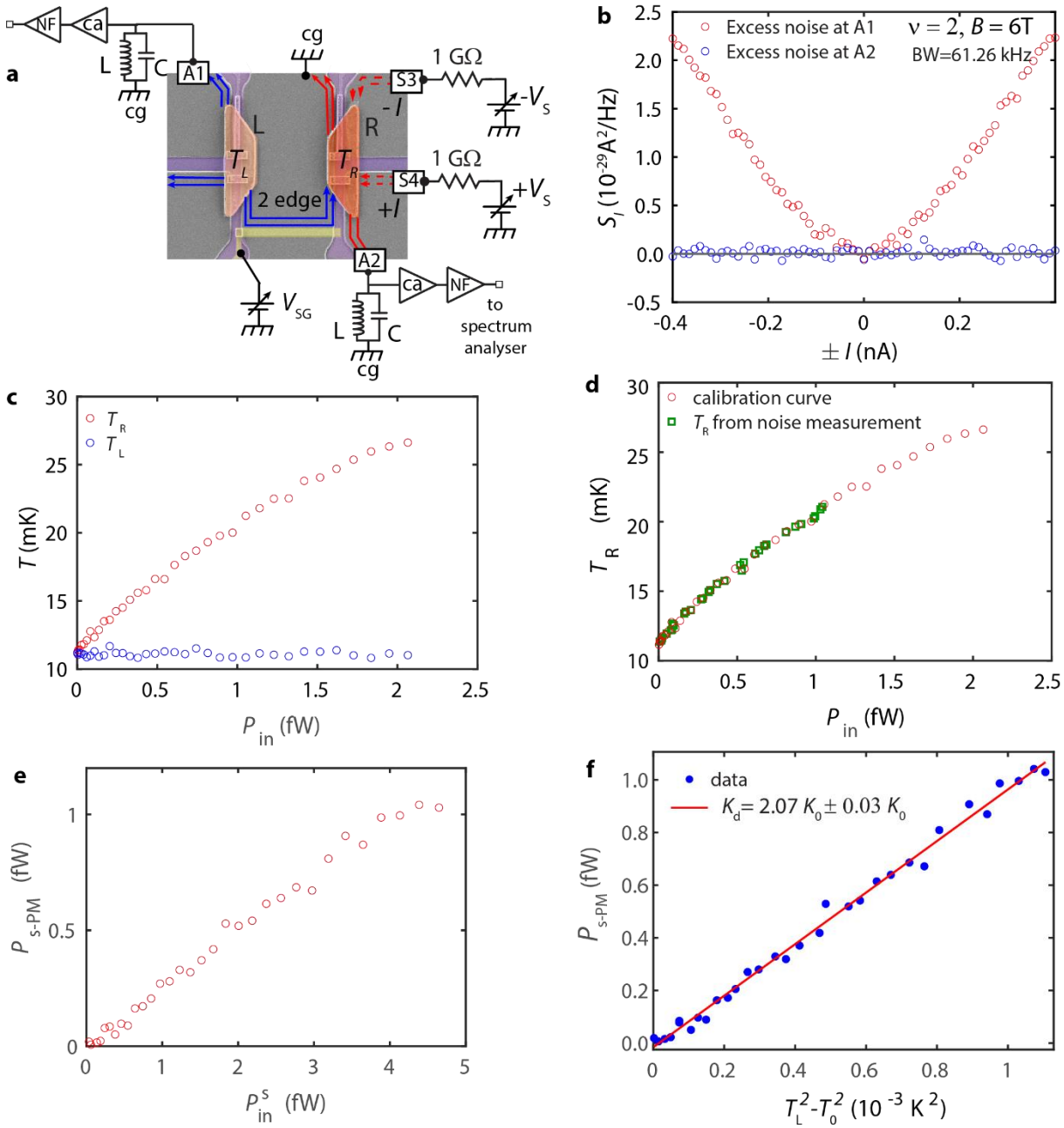

Figure SI-3: Calibration of power-meter- (a) Setup to establish the temperature vs. input power (P_{in}) calibration curve for the PM (contact R, dark red). **(b)** Excess noise (S_I) from the floating contacts plotted against injected current (I) to the PM contact R. The colors red and blue are for excess noises from contacts R and L, respectively. **(c)** Temperatures T_R (red) and T_L (blue) of the floating contacts determined from S_I as function of injected power P_{in} to the

PM. The T_R vs. P_{in} curve serves as the calibration curve. **(d)** The calibration curve (red) together with the PM temperatures (green square) from the noise measurement step to determine the arriving power ($P_{s\text{-}PM}$) to PM when the source (contact L) is heated. **(e)** $P_{s\text{-}PM}$ against the power injected P_{in}^{S} to source in the noise measurement step. **(f)** $P_{s\text{-}PM}$ as function of $T_L^2 - T_0^2$ with T_L the temperature of the source contact, for determining the thermal conductance.

SI-3: Controlling number of edge modes between the floating contacts

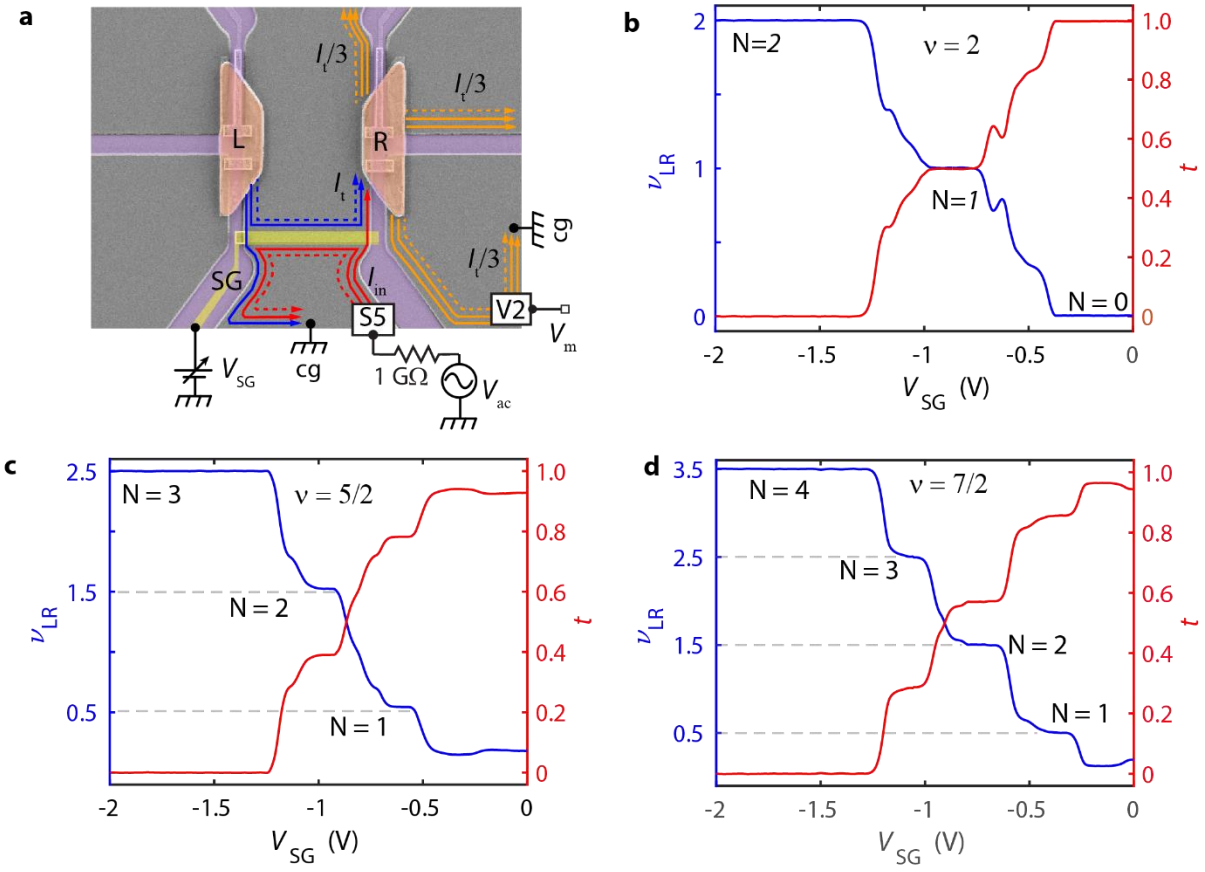

Figure SI-4: Gate responses - (a) Measurement setup for gate transmittance (t) versus gate voltage (V_{SG}) responses. **(b), (c)** and **(d)** Transmittance (t, in red) and ν_{LR} (in blue) as function of the gate voltage V_{SG} for the $\nu_{LR} = 2$, 5/2 and 7/2 states, respectively. The horizontal dashed lines mark the plateaus at ½ integer values. The edge mode number N corresponding to the plateaus are shown in the figures.

As mentioned in the main text we use the gate SG to control the number of edge modes between the floating contacts. To select appropriate gate voltages (V_{SG}) we utilize the gate transmittance (t) versus V_{SG} responses. Figure SI-4a illustrates the measurement configuration to find the transmittance t as function of V_{SG}. The gate SG (yellow shaded region) divides the middle mesa into three parts: the upper part between floating contacts (L and R), the mesa directly below SG, and the lower part. By adjusting the filling factor below SG with V_{SG}, downstream edge modes (blue arrows) from the left floating contact L can be directed to the bottom cold-ground (cg) or to the right floating contact R. To measure t, a low frequency ac current I_{in} is injected from the contact S5 (in the lower part) and is carried by downstream edge modes (red arrows) to the SG-controlled region. From here the reflected edges reach the cold ground. The transmitted edges enter floating contact R, which splits the transmitted current I_t equally between outgoing edge modes (orange arrows) of the three arms. I_t is measured from the voltage drop V_m at the probe V2 using

$$V_m = \frac{I_t}{3} R_H \qquad \text{(SI-9)}$$

where R_H is the QH resistance. Consequently, t is given by:

$$t = \frac{I_t}{I_{in}} = \frac{3V_m}{I_{in}R_H} \qquad \text{(SI-10)}$$

In this configuration, the number (N) of downstream edge modes moving from L to R is equal to the number of reflected downstream edges at SG. Therefore, t can be translated into effective filling factor (ν_{LR}) of the edge modes moving from L to R, with

$$\nu = (1-t)\,\nu_{LR} \qquad \text{(SI-11)}$$

where ν is the filling factor set by applied magnetic field. Note, ν_{LR} determine the electrical conductance $G_{LR} = \nu_{LR} G_0$ between the floating contacts. For t=0, the gate is fully pinched ($\nu_{LR} = \nu$), allowing all available modes to propagate between floating contacts. Conversely, at t=1, the gate is fully open ($\nu_{LR} = 0$), preventing any direct edge propagation between floating contacts.

Figures SI-4b to SI-4d depicts measured t (in blue) and ν_{LR} (in red) as functions of the gate voltage V_{SG} for the studied filling factors. For $\nu = 2$, we find $\nu_{LR} = 0$ (i.e. t=1), for $V_{SG} > -0.38$ V (Figure SI- 5b), indicating a fully open gate. For the even-denominator states, the gate remains fully open at V_{SG}=0 before applying any non-zero gate voltage. However, once a voltage is applied, the gate does not open fully even at V_{SG}=0. Consequently, the transmittance never returns to unity, (see Fig. SI-4c and SI-4d). This behavior is due to the hysteretic nature of the complicated SPSL-type doping in our GaAs samples. Regardless, in all cases, as V_{SG} decreases, t approaches zero after consistently passing through multiple (single for $\nu = 2$) plateaus. As a result, ν_{LR} increases and match the filling factor ν (beyond $V_{SG} < -1.3$V). These plateaus signify sequential addition of the edge modes between L and R. Therefore, to vary number of edge mode (N) in the thermal conductance measurement, gate voltages are set in the middle of these plateaus. As seen, for $\nu = 2$, a lone intermediate plateau appears at $\nu_{LR} = 1$ (t = 0.5) indicating the presence of a single integer edge mode (N=1) between L and R. In the case of even denominator states, the plateaus appear at half-integer values of ν_{LR}, as marked by the horizontal dashed lines in Figures SI-4c and SI-4d. The plateau with $\nu_{LR} = 0.5$ is for the isolated fractional ½ charged mode (N=1) with $G_{LR}=\frac{1}{2}G_0$. The subsequent plateaus appear at ν_{LR} = 1.5, 2.5 and 3.5 (ν_{LR} = 3.5 is exclusive to $\nu = 7/2$ state), indicating to inclusion of one, two and three integer edge modes, respectively, atop the ½ fractional mode (resulting in N=2,3 and 4, respectively). The edge mode numbers for corresponding to the plateaus are shown in the figures.

SI-4: Upstream thermal conductance as function of the edge mode number

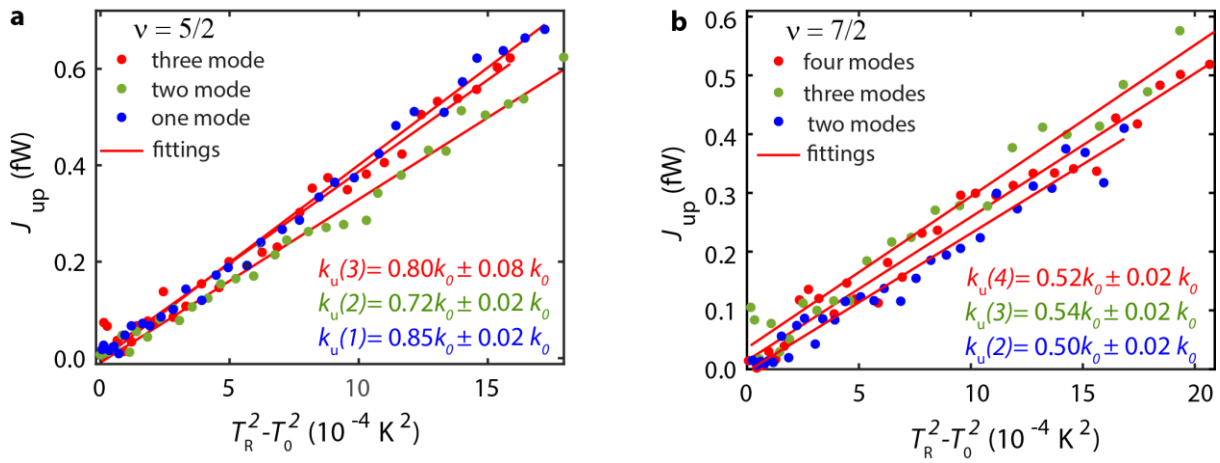

Figure SI-5: Upstream thermal conductance - (a) and **(b)**Upstream heat current J_{up} vs. $T_R^2 - T_0^2$ plots with number of edge mode (N) between the floating contacts for the $\nu = 5/2$ and $\nu = 7/2$ states, respectively. The red lines are linear fit to the plot to find the thermal conductance k_u(N). The k_u(N) values determined from the plots are color coded.

For upstream heat conductance (k_u) measurement, we reverse the roles of the floating contacts: the right floating contact R becomes the *temperature source*, and the left contact L serves as the *power-meter* (PM). Figures SI-5a and SI-5b show the upstream heat current J_{up} relative to $T_R^2 - T_0^2$ for different edge mode numbers (N) between L and R, for the ν=5/2 and ν=7/2 states, respectively. The k_u(N) values (color coded) determined from the plots are also shown in the figures. As can be seen, for both the states, the upstream heat conductance is independent of edge mode count.

SI-5: Bulk and Upstream heat conductance at *ν*=7/2

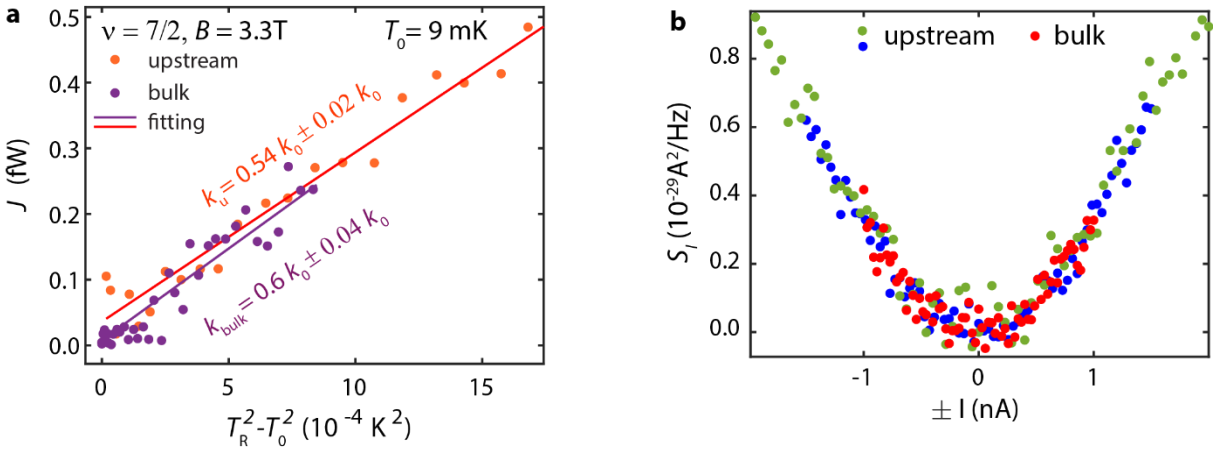

Figure SI-6: (a) heat current J vs. $T_R^2 - T_0^2$ plots for bulk and upstream heat conductance at ν=7/2. (b) Comparison of PM excess noises due bulk (red) and upstream (green, blue) heat flow at ν=7/2.

Figure SI-6a compares heat current J vs. $T_R^2 - T_0^2$ plots for bulk and upstream heat conductance at ν=7/2**.** We observe slightly higher $k_{bulk} \sim 0.6\ k_0$, compared to the average upstream $k_u \sim 0.52\ k_0$, which is unusual. However, the plot for bulk heat conductance closely flows the plot for upstream heat conductance. This alignment is more evident in Figure SI-6b comparing PM excess noise due to bulk (in red) and upstream (in blue and green) heat flows. The observed higher value can be attributed to fitting error arising from more noisy data of bulk taken at within a lower temperature range.

SI-6: Gain calibration of the cryo-amplifiers

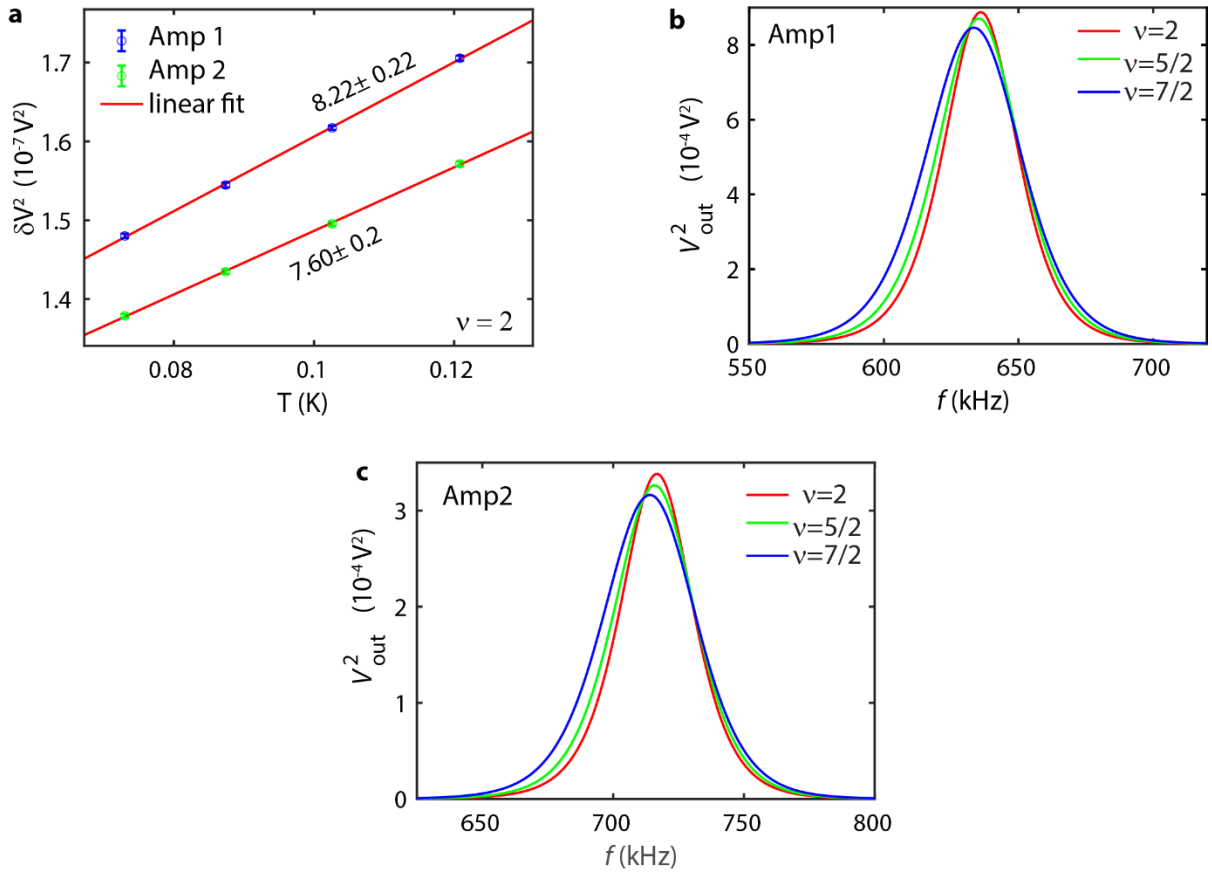

Figure SI-7: Gain calibration- (a) Measured background voltage fluctuation δV_{out}^2 as a function temperature (T), at filling factor $\nu = 2$, for both amplifiers. Red lines are the linear fits to find the slopes to determine the amplifier gains. **(b)** and **(d)** Resonance plots at different filling factors for Amp1 and Amp2, respectively. The resonance frequencies are ~634 kHz and ~717 kHz, respectively. V_{out} corresponds to the amplified output signal in response to a known high frequency signal applied to the sample.

The gains of the HEMT cryo-amplifiers vary with temperature cycle, necessitating gain calibration before conducting noise measurements. For the robust integer ν=2 state we have used equilibrium Johnson-Nyquist noise to determine the amplifier gains. The equilibrium thermal noise at any temperature T is given by $S_V = 4\, k_B T R = \langle \delta V_{th}^2 \rangle / BW$, where δV_{th}^2 is thermal

noise voltage fluctuation, k_B is Boltzmann constant, R is Quantum Hall resistance, and BW is the measurement bandwidth (~61.3 kHz). In Figure SI-6(a), the total background noises (δV_{th}^2) measured by the amplifiers are plotted against the sample temperature T, with green and red colors representing noise from the left (denoted as Amp1) and right (denoted as Amp2) amplifiers, respectively. The measured noise contains amplified thermal noise as well as the amplifiers own current and voltage noises (δV_A^2),

$$\delta V_{out}^2 = A^2 (\delta V_{th}^2 + \delta V_A^2) \qquad \text{(SI-12)}$$

However, since the amplifiers sits at 4k the amplifier noises are independent of the sample temperature. This enables determination of the gain (A) from the slope of the linear δV_{out}^2 vs, T plots, using $A=\sqrt{slope/(4\, k_B T\, R\, BW)}$**.** While measuring the 10 μm separation device, we measured gain 8.22±0.22, and 7.60±0.20 for Amp1 and Amp2, respectively, at ν=2. In the second measurement of the 30 μm separation device, Amp1 exhibited gains of 7.59±0.5, while Amp2 had gains of 5.03±0.11 at ν=2.

For the fragile even denominator states the amplifier gains are estimated by comparing the LC resonance plot areas associated to the states to that of $\nu = 2$. This method utilizes the relation between the resonance plot area, amplifier gain and measurement bandwidth given by,

$$A = \frac{1}{V_{in}} \sqrt{\frac{Area}{BW}}, \qquad \text{(SI-13)}$$

where V_{in} a frequency independent input signal to the amplifier contacts. Comparing resonance area with known gain to resonance area for unknown gain eliminates V_{in} which is difficult to measure accurately, due to capacitive losses. Figure SI-6b and SI-6c illustrates comparison of the resonance plots for both amplifiers at the studied filling factors. For the 5/2 states' measurement, Amp1 gain was ~8.7, and Amp2 had gain of ~7.41. During the 7/2 states' the gain were ~8.52 and ~5.64, respectively.

Supplementary references:

1. Melcer, R. A., Konyzheva, S., Heiblum, M. & Umansky, V. Direct determination of the topological thermal conductance via local power measurement. Nature Physics 19, 327–332 (2023).

2. Melcer, R. A. et al. Heat conductance of the quantum hall bulk. arXiv preprint arXiv:2306.14977 (2023).